Supplementary Data

A resilient MXene/CNT nano-accordion framework for anode-free sodium-metal batteries with exceptional cyclic stability

Experimental section

Reagents

Ti_3AlC_2 MAX powder (400 mesh, <38.0 μm particle size, Carbon-Ukraine), lithium fluoride (> 99.99%, Sigma-Aldrich, Korea), hydrochloric acid (35-38.0%, Daejung Chemicals & Metals, Korea), and single-walled carbon nanotubes (CNTs, MEIJO eDIPS) were obtained and utilized in their acquired state.

Synthesis

The synthesis of $Ti_3C_2T_x$/CNT NAFs was carried out in two steps, as described in the following section.

Synthesis of the $Ti_3C_2T_x$

The $Ti_3C_2T_x$ MXene was synthesized by selectively etching of aluminum (Al) from the Ti_3AlC_2 MAX phase using the modified minimally intensive layer delamination (MILD) method.[1] The etchant was prepared by adding 2.0 g of LiF to 10.0 mL of 6.0 M HCl in a Teflon vessel under stirring. Then, about 2.0 g of Ti_3AlC_2 MAX powder was slowly added into the etchant and continued the stirring at 350 rpm for 24.0 h at a temperature of 35.0 °C. After completion of the reaction, the contents were washed with DIW *via* centrifugation (5,000 rpm, 10 min per cycle) several times until the pH reached to 7. After this process, the sediment of $Ti_3C_2T_x$ MXene settled

at the bottom of the centrifuge tube is started swelling gradually. The swollen $Ti_3C_2T_x$ MXene sediment was adjusted to the desired concentration by adding the DIW and then shaken for about 90 min. Afterward, the supernatant was collected by centrifugation at 3,500 rpm for 5 min. The obtained supernatant was vacuum-filtered to obtain $Ti_3C_2T_x$ MXene films.

Synthesis of the $Ti_3C_2T_x$/CNT nano-accordion frameworks (NAFs)

Initially, about 200.0 mg of CNTs were dispersed in 50.0 mL of distilled water (DIW), followed by 30 minutes of probe sonication to obtain uniformly dispersed CNTs in DIW. After combining the aqueous dispersions of premade $Ti_3C_2T_x$ and CNTs in an 8:2 weight ratio, the dispersion was sonicated for approximately 20 minutes. After mixing the dispersion thoroughly, it was transferred into a silicone mold on a silicon wafer. Then, they were placed on a pre-cooled copper cold substrate beneath a Dewar flask holding liquid nitrogen and quenched. Finally, samples that had been quenched were freeze-dried to produce $Ti_3C_2T_x$/CNT NAFs. The $Ti_3C_2T_x$ NAFs and CNT free-standing electrodes (FSEs) were prepared similarly to $Ti_3C_2T_x$/CNT NAFs.

Characterization of the $Ti_3C_2T_x$/CNT NAFs

The prepared samples were analyzed using XRD to determine the phase purity. All measurements were carried out utilizing a Rigaku high-power powder X-ray diffractometer, Japan, with a 2θ range of 10-70^o and a scan rate of 2^o min^{-1}. Raman spectroscopy was carried out using a Renishaw inVia spectrometer equipped with a He:Ne laser (λ_{max} = 633 nm) over the wavelength range of 100-4,000 cm^{-1}. The formation of 3D $Ti_3C_2T_x$/CNT NAFs was studied by field emission scanning electron microscopy (FE-SEM, Sigma 300, JEOL). To prevent the surface of the Na-plated and stripped samples from being oxidized by air during the IMS (Ion Milling System, ArBlade 5000) process and FE-SEM (Regulus 8230, Hitachi) measurements, we employed the IMS in an inert

atmosphere to cut the sample cross-sections and then transferred them to the FE-SEM in the same atmosphere. Energy dispersive X-ray analysis (EDS) connected to an FE-SEM device was used to determine the elemental composition. The surface oxidation states of the $Ti_3C_2T_x$/CNT NAFs and Na-plated/stripped $Ti_3C_2T_x$/CNT NAF samples were studied using an X-ray photoelectron spectrometer (Thermo Scientific Inc.).

Electrochemical study of the $Ti_3C_2T_x$/CNT NAFs

All the electrochemical studies of the samples were carried out using CR2032 coin-type cells. The $Ti_3C_2T_x$/CNT NAF were pressed on a Cu foil and used as an anode host. The mass loading was fixed at 1.0 mg cm^{-2} for all the electrodes. All the cells were fabricated under an argon-filled glove box with below 0.1 ppm oxygen and moisture levels. All the asymmetric cells were fabricated using metallic Na-foil (Na-cubes, Sigma-Aldrich) as a counter electrode and 1.0 M sodium hexafluorophosphate ($NaPF_6$, ≥ 98.0%, Sigma-Aldrich) in diglyme (anhydrous, ≥ 99.5%, Sigma-Aldrich) as an electrolyte (50.0 μL). The symmetrical cells were assembled with two similar electrodes and each time 20.0% excess Na was deposited more than the required capacity on each electrode (For example, 1.2 mAh cm^{-2} for 1.0 mAh cm^{-2} symmetrical cell). Here, celgard 2400 was used as a separator. Both the asymmetric and symmetric cells were tested at different capacities at different currents. All the electrochemical measurements including plating/stripping and symmetrical cell cyclic stability studies were performed on a multichannel battery tester (WMPG1000S, WonA Tech). Electrochemical impedance spectroscopy (EIS, Metrohm Autolab) was employed to study the electrode kinetics of symmetric cells in the frequency range of 0.1 Hz to 100 kHz. The $Na_3V_2(PO_4)_3$@C was purchased from AME Energy Co. Ltd., China, and used as received. For assembling a full cell, $Na_3V_2(PO_4)_3$@C and CNTs (200.0 mg in 50.0 mL of N-

Methyl-2-pyrrolidone (NMP)) were mixed in a weight ratio of 9:1 and blade-coated on an Al foil; the cathode mass was kept at 11.0 mg cm^{-2}. The electrolyte used for full cell testing was 0.75 M $NaPF_6$ & 0.25 M sodium tetrafluoroborate ($NaBF_4$, ≥ 98.0%, Sigma-Aldrich) in dimethoxyethane (DME). Here, Whatman® glass microfiber filter (Grade GF/F) was employed as a separator. The galvanostatic charge-discharge (GCD) curves and cyclic stability studies of full cells were carried out in a potential window of 2.5-3.8 V vs. Na/Na^+ using the same battery tester.

Computational method

First-principles density functional theory (DFT) calculations were carried out using the Vienna ab initio simulation package (VASP).[2] The interaction between electrons and ions was described by the projector augmented wave (PAW) method, setting the plane-wave energy cutoff at 400 eV. The van der Waals interactions were accurately described using the vdW-DF exchange-correlation functional.[3] The MXene surface models for Na binding calculations were constructed based on 2 × 2 supercells of previously reported hexagonal unit cells of $Ti_3C_2T_x$.[4] The CNT (5×5) structures were generated using the Atomic Simulation Environment (ASE) Python toolkit.[5] The Monkhorst-Pack grid of 5 × 5 × 1 and 3 × 1 × 1 were utilized for integration in k-space for MXene and CNT models, respectively. A vacuum region of 15 Å along the surface normal direction was incorporated into all surface models, with a dipole correction scheme included. The Gaussian smearing method was employed to determine the electron occupation, with a smearing energy of 0.1 eV. Geometry optimizations were conducted until the atomic forces were less than 0.01 eV/Å and total energy convergence was below 10^{-5} eV. Bader partial charge analysis was carried out using the code from the Henkelman group.[6]

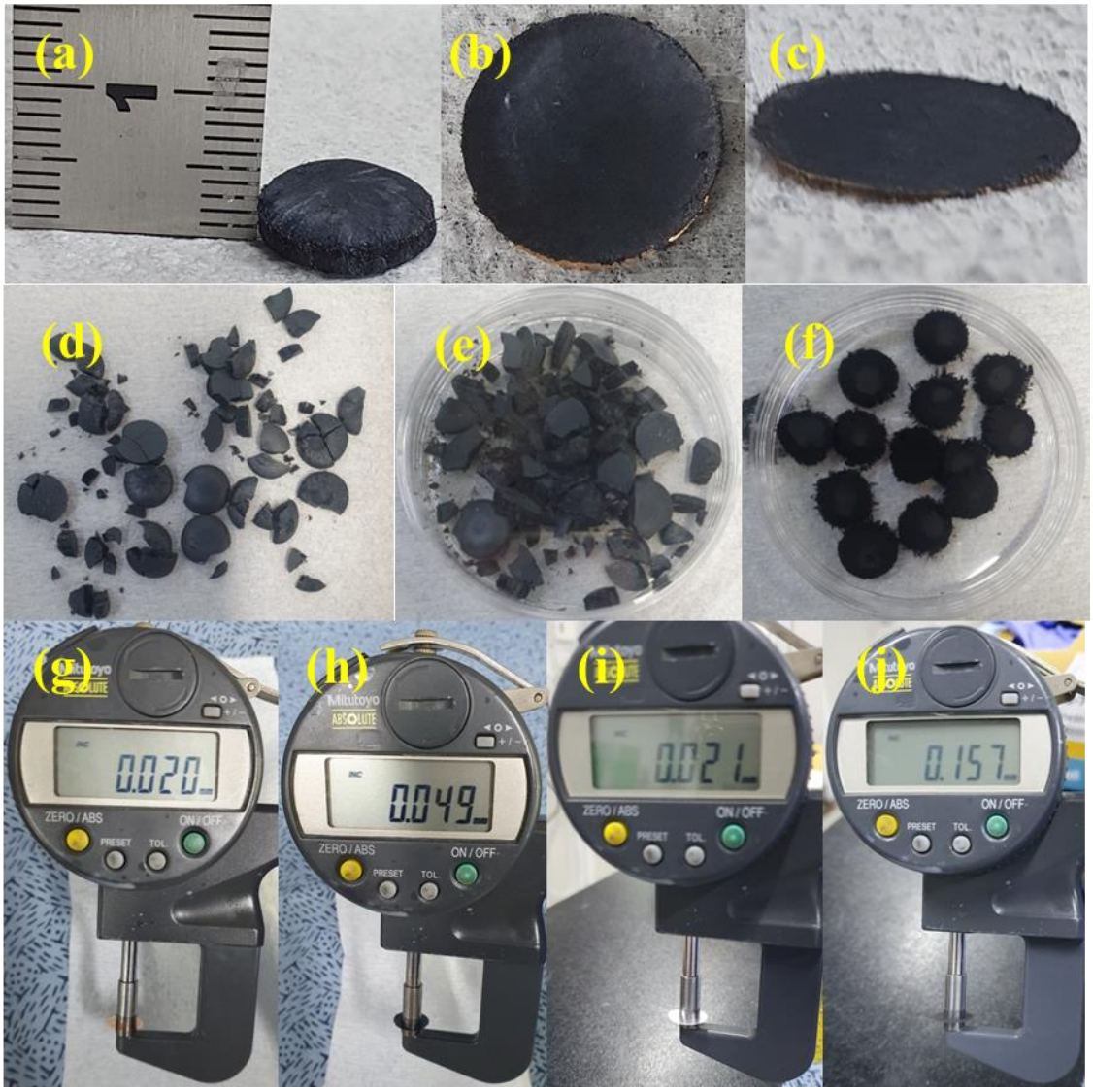

Fig. S1. Digital images of the (a) as-prepared $Ti_3C_2T_x$/CNT NAFs and (b and c) top-view and side-view of pressed $Ti_3C_2T_x$/CNT NAFs on a Cu foil, (d & e) as prepared $Ti_3C_2T_x$ NAFs and (f) CNT FSEs. Digital images of the measured thickness of the (g) pristine Cu foil, (h) pressed $Ti_3C_2T_x$/CNT NAFs on a Cu foil, (i) pristine Al coil, and (j) $Na_3V_2(PO_4)_3$@C coated on an Al foil.

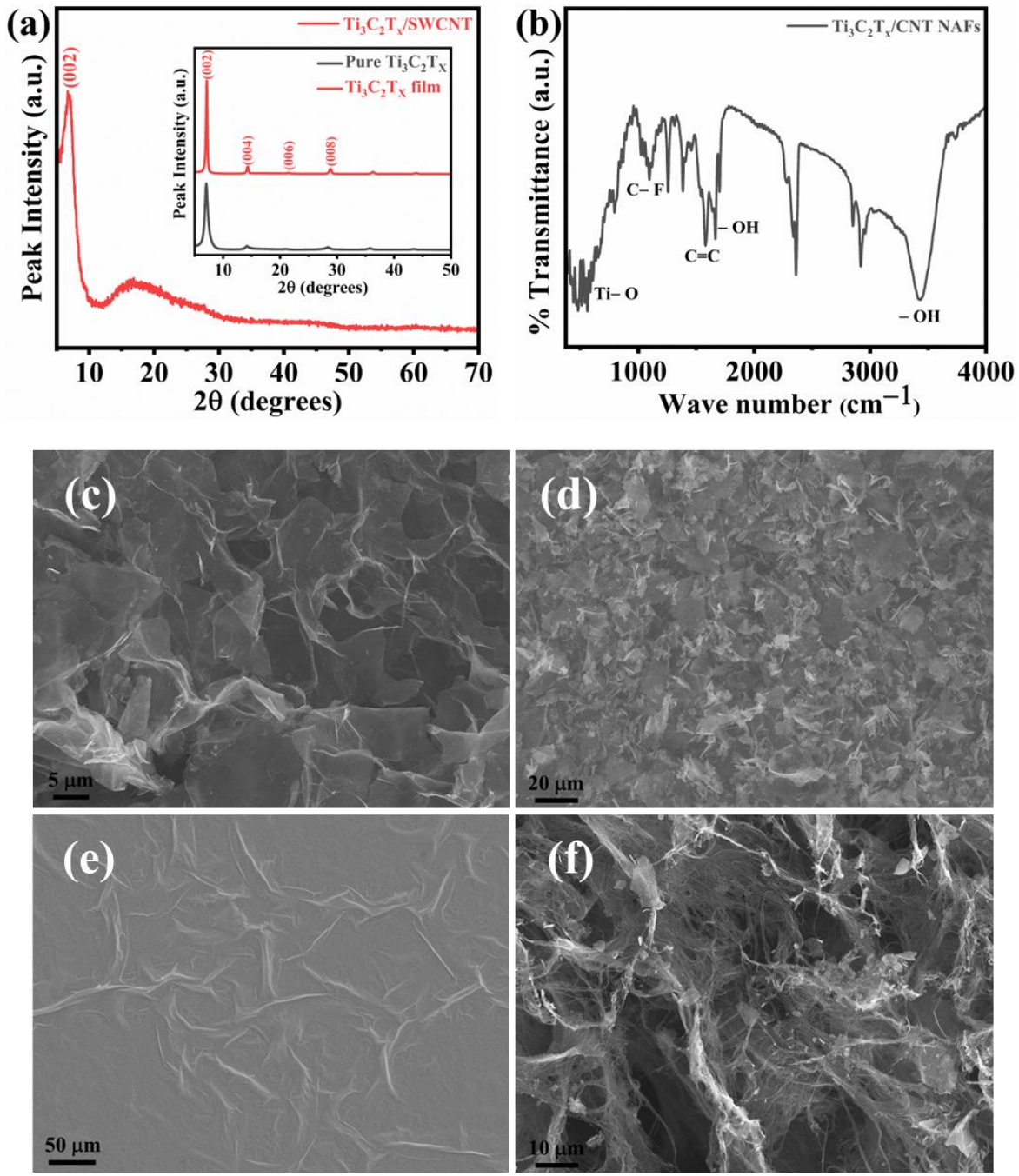

Fig. S2. (a) XRD spectrum of $Ti_3C_2T_x$/CNT NAF sample (Inset shows the XRD spectrum of pure $Ti_3C_2T_x$ and $Ti_3C_2T_x$ film). (b) FT-IR spectrum of $Ti_3C_2T_x$/CNT NAF sample. FE-SEM images of (c) pure $Ti_3C_2T_x$, (d) $Ti_3C_2T_x$ NAFs, (e) $Ti_3C_2T_x$ film, and (f) CNT FSEs.

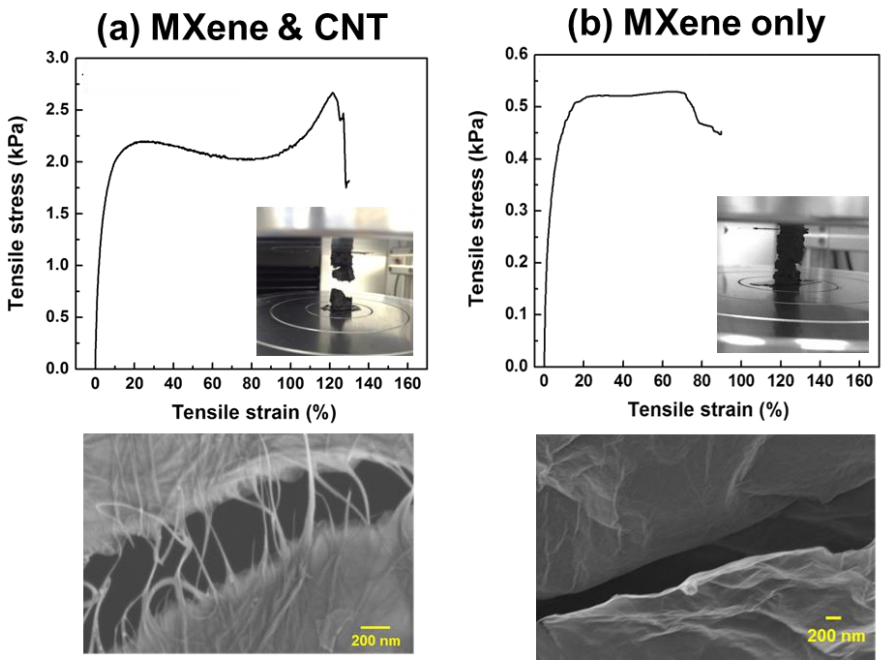

Fig. S3. The tensile stress-strain curves using a universal testing machine and their SEM image at the torn area of (a) $Ti_3C_2T_x$/CNT composite network and (b) $Ti_3C_2T_x$ MXene-only network.

The mechanical properties of the uncompressed cellular network of only the $Ti_3C_2T_x$ MXene 2D material and the cellular network containing $Ti_3C_2T_x$ MXene and CNT in a 5:5 ratio were tested for mechanical stability through a tensile test using UTM equipment. The $Ti_3C_2T_x$/CNT 2D/1D network showed much higher toughness compared to the 2D $Ti_3C_2T_x$ material-only network (**Fig. S3**). The subsequent SEM observation of the torn area also showed that the 2D $Ti_3C_2T_x$ material showed a clean boundary, but in the $Ti_3C_2T_x$/CNT 2D/1D composite material, the CNTs were still connected at the torn boundary and showed high mechanical toughness. In addition, in the compression process for use as an electrode, as shown in (b-e) of **Fig. S1**, the $Ti_3C_2T_x$/CNT 2D/1D system is capable of stable compression, but the structure of only 2D $Ti_3C_2T_x$ materials showed low mechanical stability when compressed, making it difficult to use as an electrode. This shows that the $Ti_3C_2T_x$/CNT 2D/1D composite network in this study has more stable properties even under mechanical deformation.

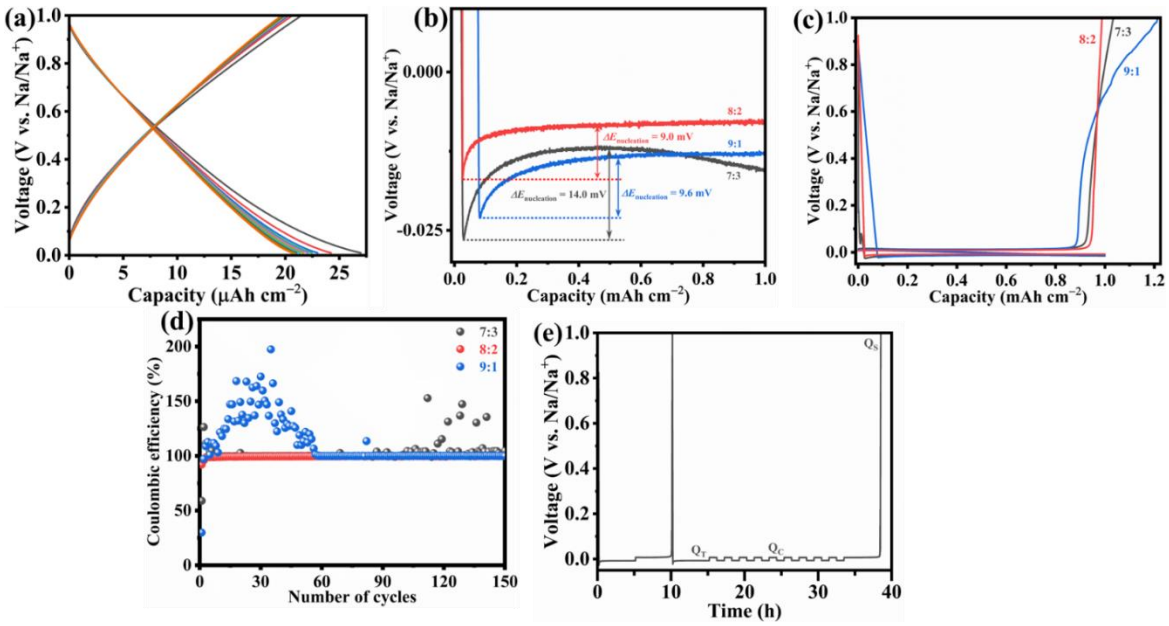

Fig. S4. (a) precycling of $Ti_3C_2T_x$/CNT NAF (8:2) sample. (b) Nucleation overpotential, (c) Na plating and stripping, and (d) CE plots of $Ti_3C_2T_x$/CNT NAFs with a capacity of 1.0 mAh cm^{-2} at 1.0 mA cm^{-2} ($Ti_3C_2T_x$:CNT = 7:3, 8:2 & 9:1). (e) Voltage *vs.* time plot of $Ti_3C_2T_x$/CNT NAFs/Na asymmetric cells.

To understand the better electrochemical performance of $Ti_3C_2T_x$/CNT NAFs, we have chosen three compositions with $Ti_3C_2T_x$:CNT = 7:3, 8:2 & 9:1 and examined their electrochemical performance (**Figs. S4b-d**). The $Ti_3C_2T_x$/CNT NAF samples with $Ti_3C_2T_x$:CNT ratios of 7:3, 8:2 & 9:1 show nucleation overpotential of 14.0, 9.0, and 9.6 mV, respectively (**Fig. S4b**). The $Ti_3C_2T_x$/CNT NAF sample with a $Ti_3C_2T_x$:CNT ratio of 8:2 shows better plating and stripping as compared to that of 7:3 and 9:1 (**Fig. S4c**). The $Ti_3C_2T_x$/CNT NAF samples with $Ti_3C_2T_x$:CNT ratios of 7:3 & 9:1 show large fluctuation in their CEs as compared to that of the sample with 8:2 (**Fig. S4d**). Among the three samples, the $Ti_3C_2T_x$/CNT NAF sample with a $Ti_3C_2T_x$:CNT ratio of 8:2 shows better electrochemical performance and we have utilized this composition for further experiments in our electrochemical analysis.

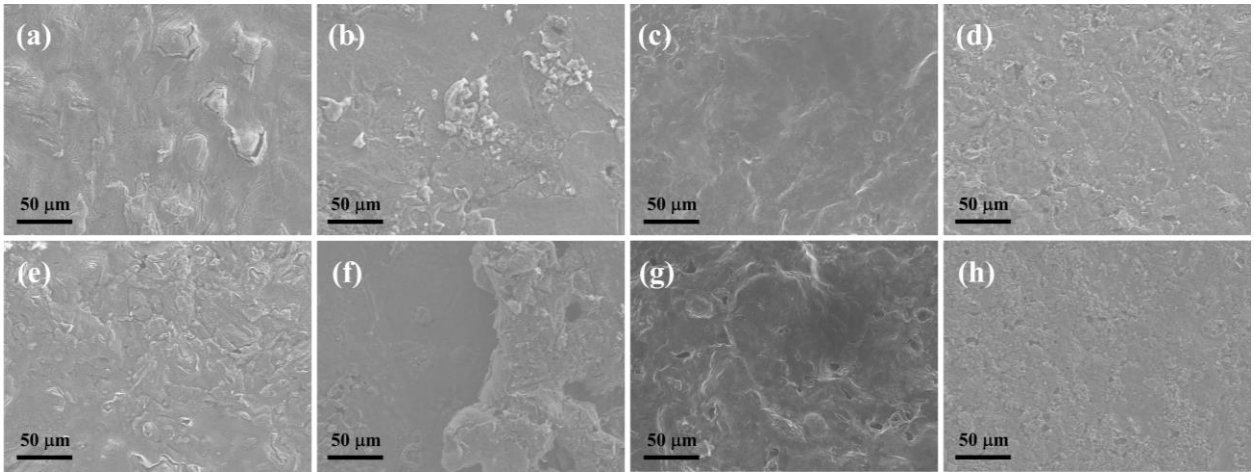

Fig. S5. Top-view FE-SEM images of (a) pristine Cu, (b) $Ti_3C_2T_x$ film, (c) CNT FSEs, and (d) $Ti_3C_2T_x$/CNT NAFs in the first cycle of plating, and (e) pristine Cu, (f) $Ti_3C_2T_x$ film, (g) CNT FSEs, and (h) $Ti_3C_2T_x$/CNT NAFs in the fiftieth cycle of plating with a capacity of 3.0 mAh cm^{-2} at 3.0 mA cm^{-2}.

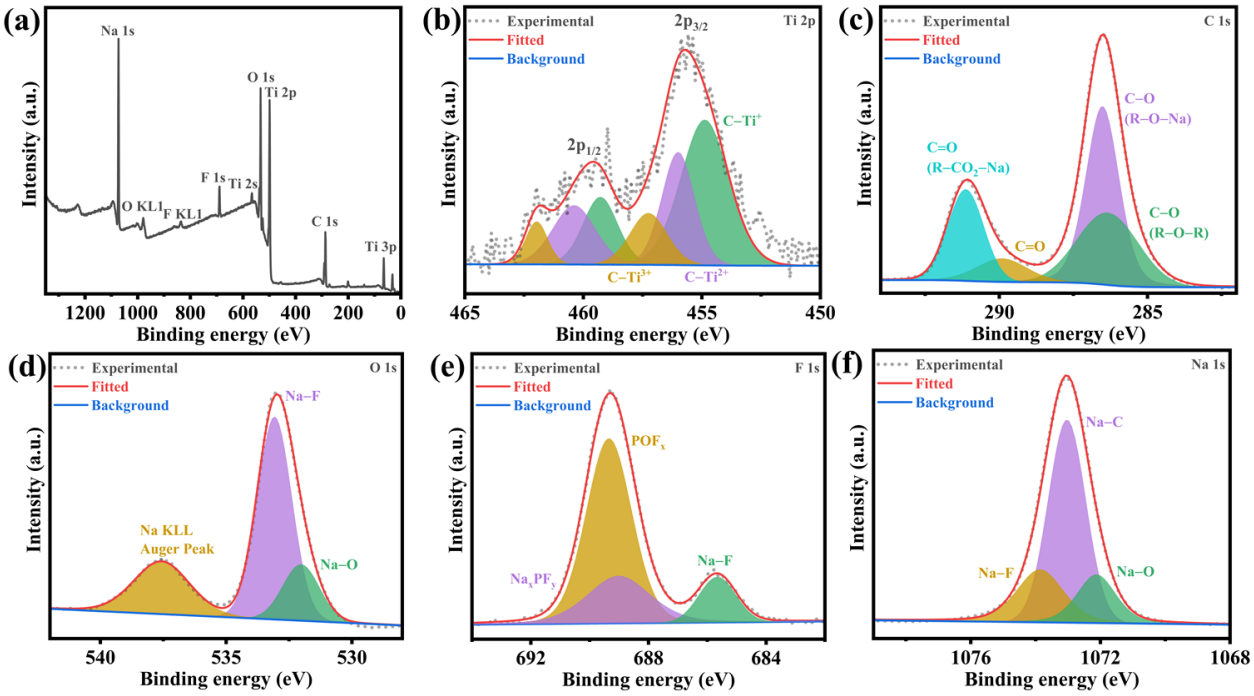

Fig. S6. (a) XPS survey spectrum and high-resolution XPS spectrums of the (b) Ti 2p, (c) C 1s, (d) O1s, (e) F1s, and (f) Na 1s of the $Ti_3C_2T_x$/CNT NAF sample after fifty plating and stripping cycles.

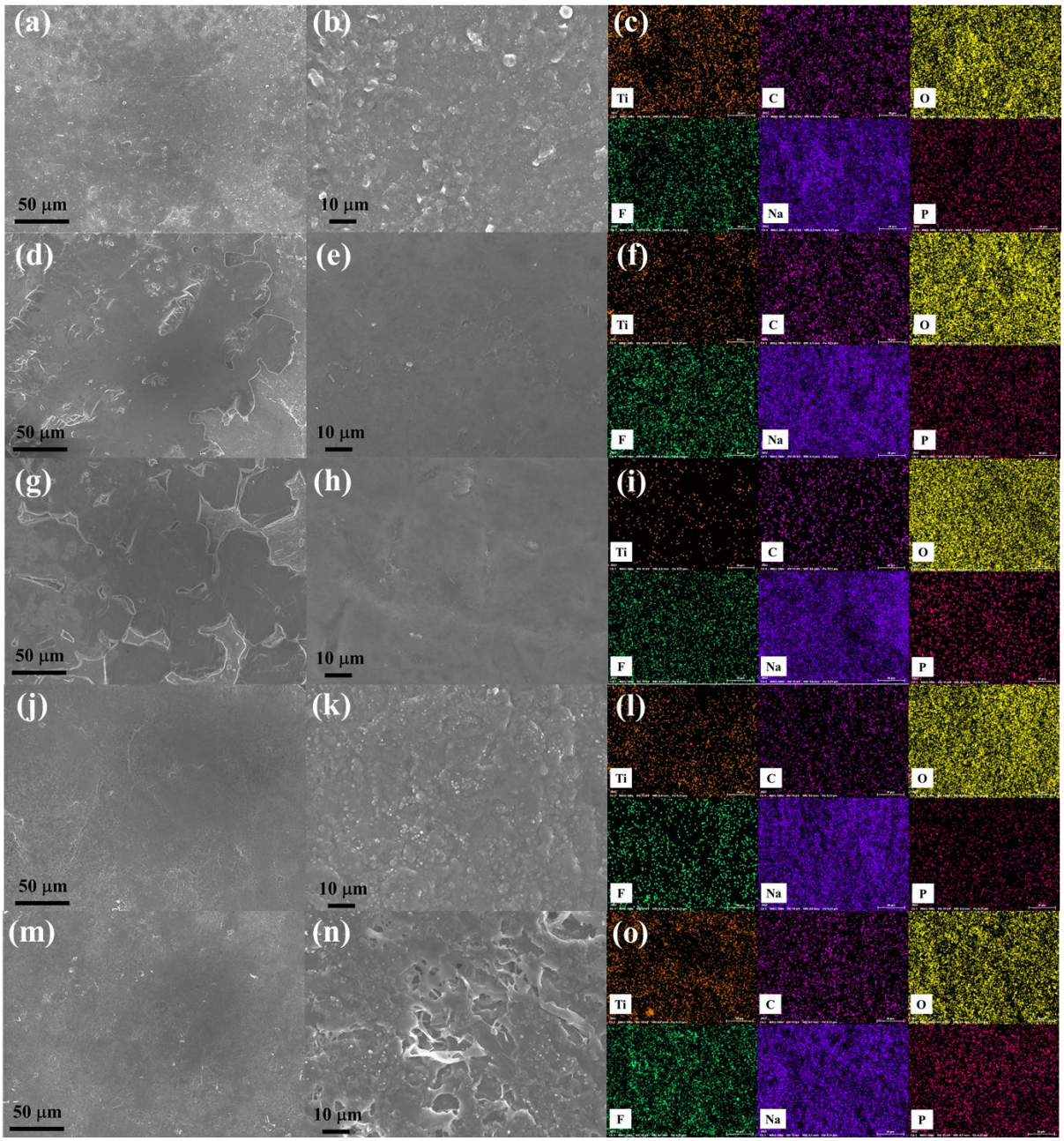

Fig. S7. Top-view FE-SEM images of $Ti_3C_2T_x$/CNT NAFs at low and high magnifications. (a and b) plating at 1.0 mAh cm^{-2}, (d and e) plating at 3.0 mAh cm^{-2}, (g and h) plating at 5.0 mAh cm^{-2}, (j and k) stripping to 3.0 mAh cm^{-2}, and (m and n) stripping to 1.0 V *vs.* Na/Na^+. (c, f, i. l, and o) Top-view EDS color mapping of Ti, C, O, F, Na, and P during plating and stripping states of $Ti_3C_2T_x$/CNT NAFs.

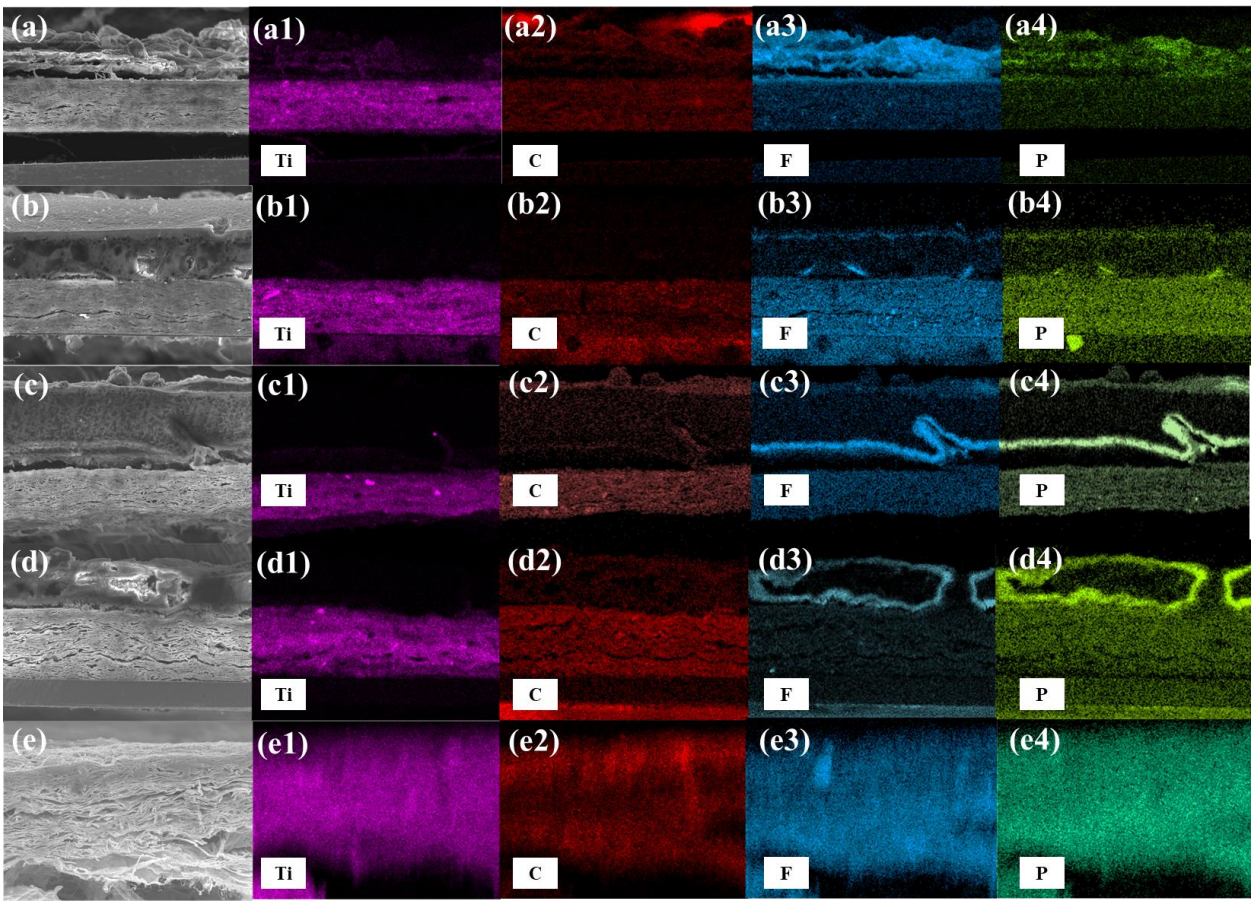

Fig. S8. Cross-sectional-view FE-SEM and EDS color mapping of Ti, C, O, F, and P elements during plating and stripping states of $Ti_3C_2T_x$/CNT NAFs. (a-a4) plating at 1.0 mAh cm^{-2}, (b-b4) plating at 3.0 mAh cm^{-2}, (c-c4) plating at 5.0 mAh cm^{-2}, (d-d4) stripping to 3.0 mAh cm^{-2}, and (e-e4) stripping to 1.0 V *vs.* Na/Na^+.

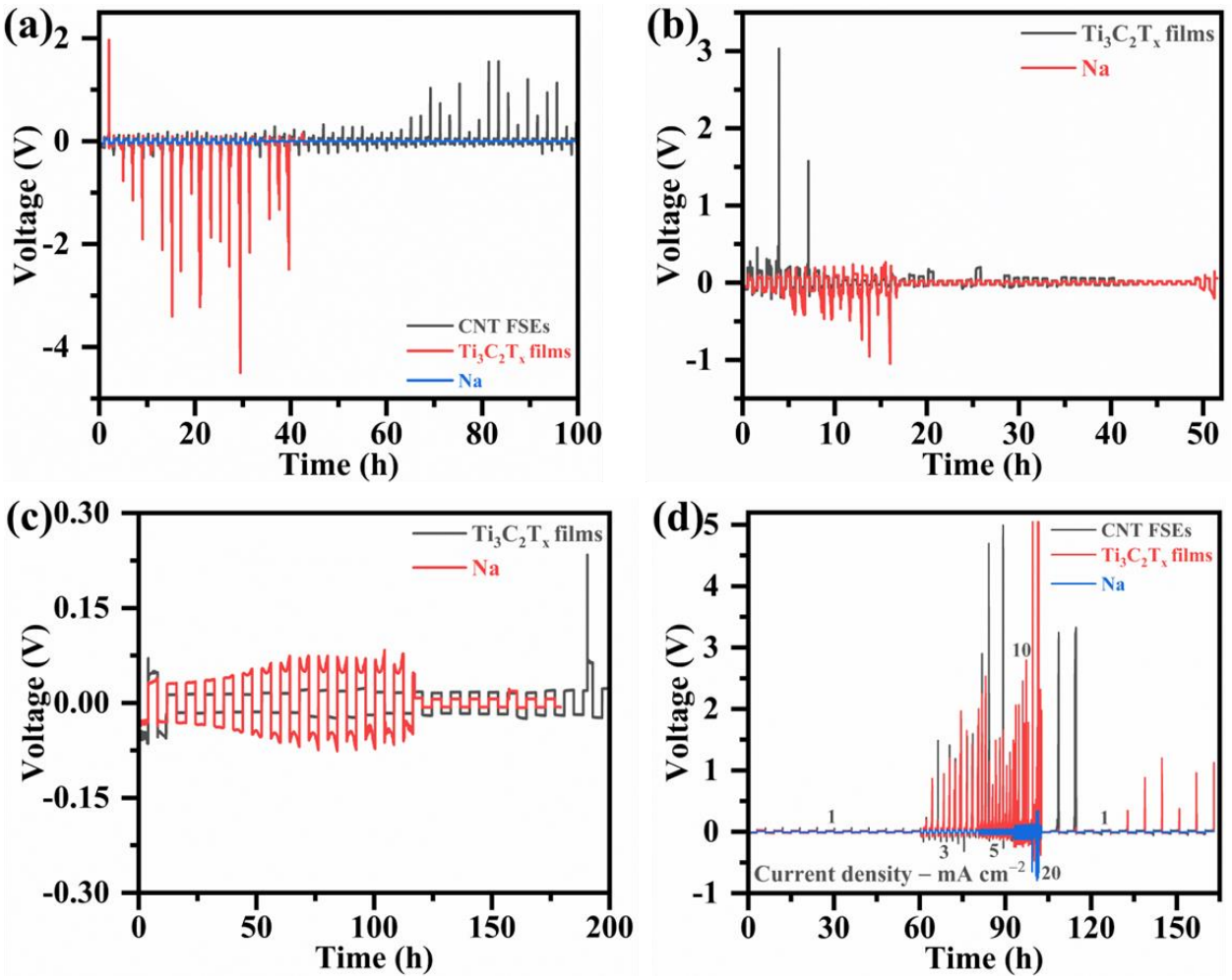

Fig. S9. Cycling performance of CNT FSEs//CNT FSEs, $Ti_3C_2T_x$ film//$Ti_3C_2T_x$ film, and Na//Na symmetric cells at (a) capacity of 3.0 mAh cm^{-2} at 3.0 mA cm^{-2}. Cycling performance of $Ti_3C_2T_x$ film//$Ti_3C_2T_x$ film and Na//Na symmetric cells at (b) capacity of 5.0 mAh cm^{-2} at 10.0 mA cm^{-2} and (c) capacity of 20.0 mAh cm^{-2} at 5.0 mA cm^{-2}. (d) rate performance of CNT FSEs//CNT FSEs, $Ti_3C_2T_x$ film//$Ti_3C_2T_x$ film, and Na//Na symmetric cells at a current of 1-20 mA cm^{-2}.

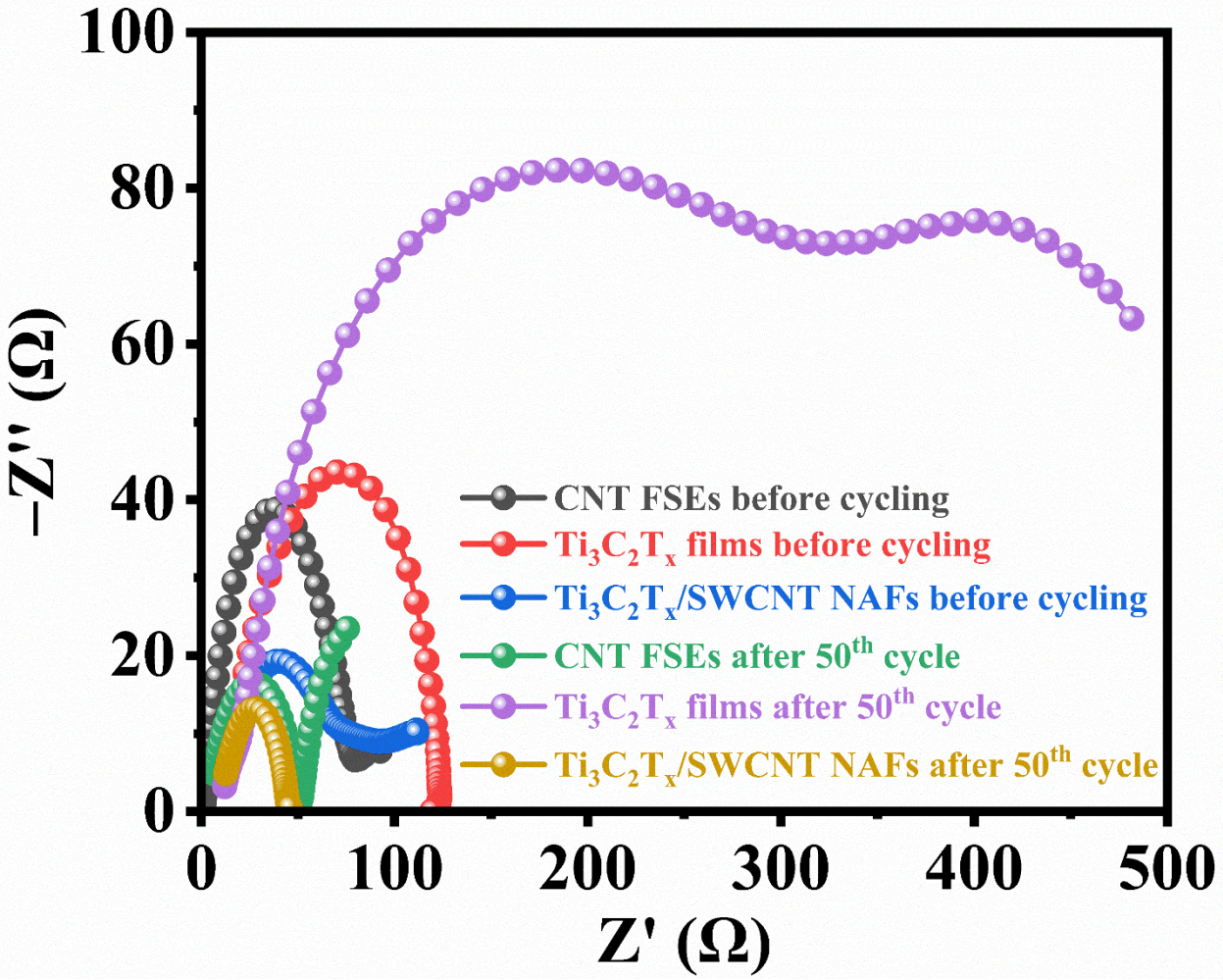

Fig. S10. EIS spectra of $Ti_3C_2T_x$ film//$Ti_3C_2T_x$ film and $Ti_3C_2T_x$/CNT NAFs //$Ti_3C_2T_x$/CNT NAFs symmetric cells at first and fiftieth cycles.

The electrochemical impedance spectroscopy (EIS) is used to examine the electrode kinetics of the $Ti_3C_2T_x$/CNT NAFs and $Ti_3C_2T_x$ film symmetric cells before and after the fiftieth cycle, and these results are depicted in Figure S9. After the fiftieth cycle, the ohmic resistance (R_s) of $Ti_3C_2T_x$/CNT NAFs decreased from 15.5 Ω to 12.6 Ω, whereas that of $Ti_3C_2T_x$ film decreased from 20.7 Ω to 12.1 Ω. The R_s of CNT FSEs slightly increased to 6.5 Ω from 1.4 Ω. However, after the fiftieth cycle, the charge transfer resistance (R_{ct}) in a $Ti_3C_2T_x$ film symmetric cell increases abruptly from 102.7 Ω to 469.7 Ω; this may be due to the growth of mossy-type dendrites on its

surface. On the other side, the decrease in R_{ct} of $Ti_3C_2T_x$/CNT NAFs (from 78.2 Ω to 32.1 Ω) and CNT FSEs (from 76.7 Ω to 44.5 Ω) implies the formation of stable SEI over the surface,[7] which can greatly reduce the Na nucleation energy barrier during cycling and hence quickens the Na^+/electron transfer at the interface of the electrode and the electrolyte. To check the better conductivity of $Ti_3C_2T_x$/CNT NAFs, we have calculated the conductivity using EIS before and after the 50^{th} cycle. The conductivity of $Ti_3C_2T_x$/CNT NAFs before and after the 50^{th} cycle was calculated to be 4.61×10^{-4} and 4.13×10^{-4} $\Omega^{-1}cm^{-1}$, respectively, suggesting better conductivity during cycling. Our results indicate that $Ti_3C_2T_x$/CNT NAFs are suitable hosts for Na deposition at high currents and capacities. The $Ti_3C_2T_x$/CNT NAFs are advantageous for inhibiting the formation of mossy-type dendrites during cycling and efficiently sustaining the volume changes compensated by nanometer-sized CNTs.

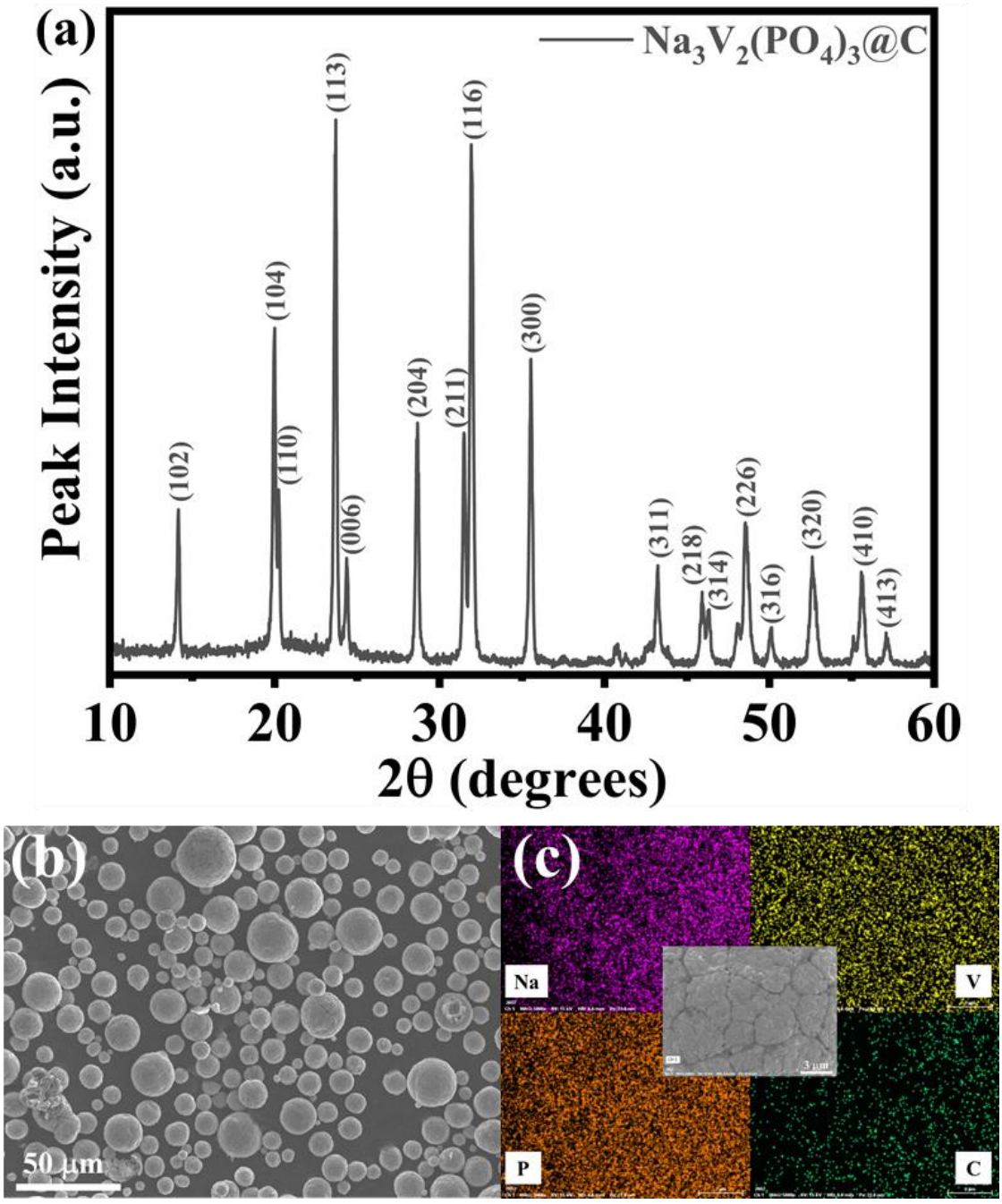

Fig. S11. (a) XRD spectra of $Na_3V_2(PO_4)_3$@C sample. (b) FE-SEM image of $Na_3V_2(PO_4)_3$@C sample. (c) EDS color mapping of $Na_3V_2(PO_4)_3$@C sample.

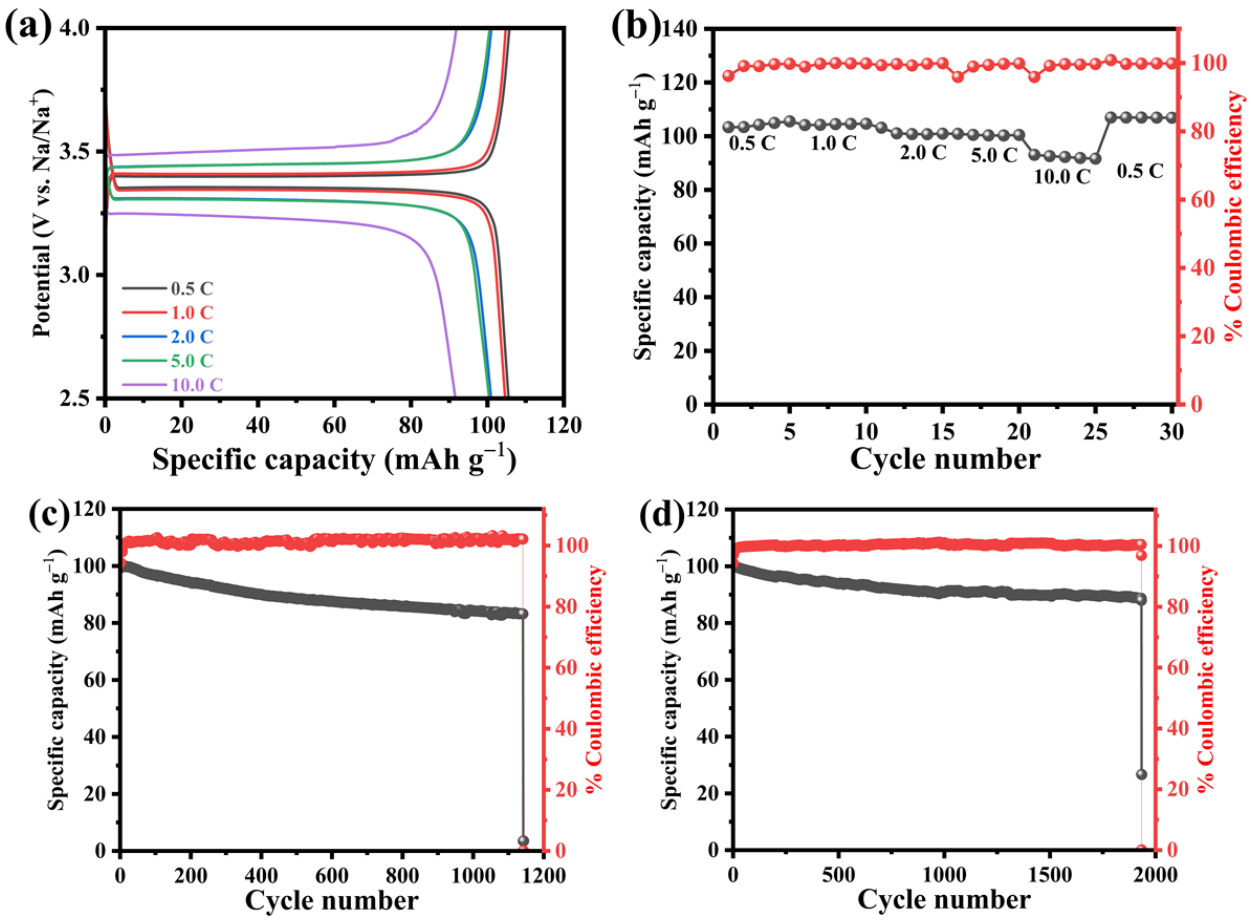

Fig. S12. (a) GCD plot of the Na//$Na_3V_2(PO_4)_3$@C cell. (b) Rate capability plot of the Na//$Na_3V_2(PO_4)_3$@C cell. (c and d) Cyclic stability plots of Na//$Na_3V_2(PO_4)_3$@C cells at 2.0 and 5.0 C, respectively.

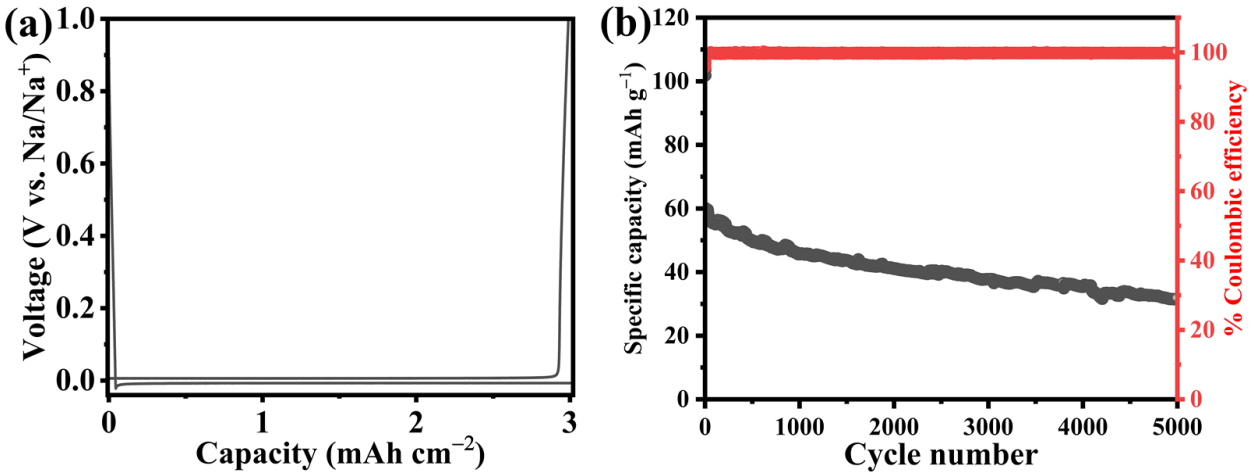

Fig. S13. (a) Preconditioning process of anode-free $Ti_3C_2T_x$/CNT NAFs/Al. (b) Cyclic stability plot of $Ti_3C_2T_x$/CNT NAFs/Al//$Na_3V_2(PO_4)_3$@C cell at 10.0 C.

Table S1. Comparison of the asymmetric cell performance of $Ti_3C_2T_x$/CNT NAFs/Na with previously reported $Ti_3C_2T_x$-based materials.

Material	Electrolyte	Current (mA cm^{-2})	Areal capacity (mAh cm^{-2})	Cycle numbers (hours)	Coulombic efficiency	Reference
Ti_3C_2@g-C_3N_4	1.0 M $NaPF_6$ in diglyme	0.5	1.0	400 (1600)	99.9%	[7]
		1.0	1.0	300 (600)	99.7%	
		3.0	3.0	200 (400)	99.7%	
CT-Sn(II)@Ti_3C_2	1.0 M $NaPF_6$ in diglyme	1.0	1.0	300 (600)	99.7%	[8]
		3.0	3.0	200 (400)	99.7%	
		5.0	5.0	200 (400)	98.8%	
		10.0	3.0	100 (60)	98.5%	
1D/2D $Na_3Ti_5O_{12}$- Ti_3C_2	1.0 M $NaPF_6$ in diglyme	3.0	3.0	300 (600)	99.4%	[9]
		10.0	5.0	200 (200)	98.8%	
h-Ti_3C_2/CNTs	1.0 M $NaCF_3SO_3$ in diglyme	1.0	1.0	1000 (2000)	99.2%	[10]
$Ti_3C_2T_x$-CC	1.0 M $NaPF_6$ in diglyme	1.0	8.0	56 (900)	98.5%	[11]
$Ti_3C_2T_x$-melamine foam	1.0 M $NaPF_6$ in diglyme	8.0	8.0	540 (270)	99.0%	[12]
		10.0	10.0	300 (150)	99.0%	
Mg(II)@Ti_3C_2	1.0 M $NaPF_6$ in EC/DEC with 5.0% FEC	1.0	1.0	90 (180)	-	[13]
rGO/Ti_3C_2	1.0 M $NaPF_6$ in diglyme	0.5	1.0	700 (2800)	99.5%	[14]
$Ti_3C_2T_x$/CNT NAFs	1.0 M $NaPF_6$ in diglyme	1.0	1.0	450 (900)	99.7%	**Present work**
		3.0	3.0	250 (500)	99.5%	
		2.5	5.0	300 (1200)	99.0%	

Table S2. Comparison of the symmetric cell performance of $Ti_3C_2T_x$/CNT NAFs/Na with previously reported $Ti_3C_2T_x$-based materials.

Material	Electrolyte	Predeposited Na (mAh cm^{-2})	Current (mA cm^{-2})	Areal capacity (mAh cm^{-2})	Hours (Overpotential, mV)	Reference
Ti_3C_2@g-C_3N_4	1.0 M $NaPF_6$ in diglyme	3.0	1.0	1.0	700 (11)	[7]
CT-Sn(II)@Ti_3C_2	1.0 M $NaPF_6$ in diglyme	3.0	3.0	1.0	134 (20)	[8]
			3.0	3.0	600 (35)	
		5.0	5.0	3.0	240 (54)	
1D/2D $Na_3Ti_5O_{12}$- Ti_3C_2	1.0 M $NaPF_6$ in diglyme	-	3.0	3.0	800 (60)	[9]
			5.0	20.0	320 (77.5)	
h-Ti_3C_2/CNTs	1.0 M $NaCF_3SO_3$ in diglyme	-	1.0	1.0	4000 (110)	[10]
			3.0	3.0	1200 (80)	
			5.0	5.0	460 (100)	
			10.0	1.0	80 (130)	
$Ti_3C_2T_x$-CC	1.0 M $NaPF_6$ in diglyme	-	5.0	1.0	370 (20)	[11]
$Ti_3C_2T_x$-melamine foam	1.0 M $NaPF_6$ in diglyme	12.0	10.0	10.0	720 (-)	[12]
Mg(II)@Ti_3C_2	1.0 M $NaPF_6$ in EC/DEC with 5.0% FEC	8.0	0.5	0.5	200 (-)	[13]
rGO/Ti_3C_2	1.0 M $NaPF_6$ in diglyme	-	1.0	1.0	1700 (34)	[14]
			3.0	1.0	1700 (200)	
$Ti_3C_2T_x$/CNT NAFs	1.0 M $NaPF_6$ in diglyme	3.6	3.0	3.0	1500 (12)	**Present work**
		6.0	10.0	5.0	1500 (58)	
		24.0	5.0	20.0	1200 (130)	

Table S3. Comparison of the full cell performance of anode-free $Ti_3C_2T_x$/CNT NAFs-Na-SEI//$Na_3V_2(PO_4)_3$@C with previously reported $Na_3V_2(PO_4)_3$-based cathode anode-free/anode-less SMBs.

Material	Electrolyte	Predeposited Na (mAh cm^{-2})	Capacity mAh g^{-1} (C-rate)	Cycle number	Capacity retention	Reference
Ti_3C_2@g-C_3N_4	1.0 M $NaPF_6$ in diglyme	3.0	95.0 (2.0)	800	91.4%	[7]
CT-Sn(II)@Ti_3C_2	1.0 M $NaClO_4$ in EC/DEC	3.0	95.0 (1.0)	200	91.8%	[8]
1D/2D $Na_3Ti_5O_{12}$- Ti_3C_2	1.0 M $NaClO_4$ in EC/PC	3.0	102.0 (1.0)	140	78.5%	[9]
$Ti_3C_2T_x$-melamine foam	1.0 M $NaClO_4$ in PC with 5.0% FEC	-	98.0 (1.0)	500	75.5%	[12]
Mg(II)@Ti_3C_2	1.0 M $NaPF_6$ in EC/DEC with 5.0% FEC	8.0	96.0 (2.0)	280	98.8%	[13]
rGO/Ti_3C_2	1.0 M $NaPF_6$ in diglyme	2.4	98.3 (0.5)	280	88.3%	[14]
OCF	1.0 M $NaPF_6$ in diglyme	1.0	98.0 (1.0)	200	90.9%	[15]
C@Sb@Cu	1.0 M $NaClO_4$ in PC with 5.0% FEC	6.0	94.5 (1.0)	500	95.0%	[16]
Sn	1.0 M $NaPF_6$ in diglyme	-	83.0 (1.0)	50	90.0%	[17]
Anode-free carbon black@Bi	1.0 M $NaPF_6$ in diglyme	-	96.0 (0.33)	100	82.5%	[18]
Anode-free PC-CFe	1.0 M $NaPF_6$ in diglyme	-	106.0 (0.55)	100	97.0%	[19]

Anode-free O-CCF	1.0 M $NaPF_6$ in diglyme	-	107.6 (0.4)	100	96.0%	[20]
Anode-free Al-Cu@C	1.0 M $NaPF_6$ in diglyme	-	102.0 (1.0)	50	76.5%	[21]
Anode-free $Ti_3C_2T_x$/CNT NAFs/Cu	0.75 M $NaPF_6$ and 0.25 M $NaBF_4$ in dimethoxyethane	-	96.9 (2.0)	100 2,500	94.1% 53.8%	**Present work**
		-	90.8 (5.0)	100 2,500 5,000	90.9% 55.2% 43.4%	
Anode-free $Ti_3C_2T_x$/CNT NAFs/Al	0.75 M $NaPF_6$ and 0.25 M $NaBF_4$ in dimethoxyethane	-	60.0 (10.0)	100 2,500 5,000	92.0% 67.2% 52.3%	

References

[1] M. Alhabeb, K. Maleski, B. Anasori, P. Lelyukh, L. Clark, S. Sin, Y. Gogotsi, Guidelines for Synthesis and Processing of Two-Dimensional Titanium Carbide ($Ti_3C_2T_x$ MXene), Chem. Mater. 29 (2017) 7633–7644. https://doi.org/10.1021/acs.chemmater.7b02847.

[2] G. Kresse, J. Furthmüller, Efficient Iterative Schemes for ab initio Total-Energy Calculations using a Plane-Wave Basis Set, Phys. Rev. B. 54 (1996) 11169–11186. https://doi.org/10.1103/PhysRevB.54.11169.

[3] M. Dion, H. Rydberg, E. Schröder, D.C. Langreth, B.I. Lundqvist, Van der Waals Density Functional for General Geometries, Phys. Rev. Lett. 92 (2004) 246401. https://doi.org/10.1103/PhysRevLett.92.246401.

[4] R. Cheng, T. Hu, H. Zhang, C. Wang, M. Hu, J. Yang, C. Cui, T. Guang, C. Li, C. Shi, P. Hou, X. Wang, Understanding the Lithium Storage Mechanism of $Ti_3C_2T_x$ MXene, J. Phys. Chem. C. 123 (2019) 1099–1109. https://doi.org/10.1021/acs.jpcc.8b10790.

[5] A.H. Larsen, J.J. Mortensen, J. Blomqvist, I.E. Castelli, R. Christensen, M. Dułak, J. Friis, M.N. Groves, B. Hammer, C. Hargus, E.D. Hermes, P.C. Jennings, P.B. Jensen, J. Kermode, J.R. Kitchin, E.L. Kolsbjerg, J. Kubal, K. Kaasbjerg, S. Lysgaard, J.B. Maronsson, T. Maxson, T. Olsen, L. Pastewka, A. Peterson, C. Rostgaard, J. Schiøtz, O. Schütt, M. Strange, K.S. Thygesen, T. Vegge, L. Vilhelmsen, M. Walter, Z. Zeng, K.W. Jacobsen, The Atomic Simulation Environment—a Python Library for Working with Atoms, J. Phys. Condens. Matter. 29 (2017) 273002. https://doi.org/10.1088/1361-648X/aa680e.

[6] G. Henkelman, A. Arnaldsson, H. Jónsson, A Fast and Robust Algorithm for Bader

Decomposition of Charge Density, Comput. Mater. Sci. 36 (2006) 354–360. https://doi.org/10.1016/j.commatsci.2005.04.010.

[7] C. Bao, J. Wang, B. Wang, J. Sun, L. He, Z. Pan, Y. Jiang, D. Wang, X. Liu, S.X. Dou, J. Wang, 3D Sodiophilic Ti_3C_2 MXene@g-C_3N_4 Hetero-Interphase Raises the Stability of Sodium Metal Anodes, ACS Nano. 16 (2022) 17197–17209. https://doi.org/10.1021/acsnano.2c07771.

[8] J. Luo, C. Wang, H. Wang, X. Hu, E. Matios, X. Lu, W. Zhang, X. Tao, W. Li, Pillared MXene with Ultralarge Interlayer Spacing as a Stable Matrix for High Performance Sodium Metal Anodes, Adv. Funct. Mater. 29 (2019) 1805946. https://doi.org/10.1002/adfm.201805946.

[9] J. Luo, X. Lu, E. Matios, C. Wang, H. Wang, Y. Zhang, X. Hu, W. Li, Tunable MXene-Derived 1D/2D Hybrid Nanoarchitectures as a Stable Matrix for Dendrite-Free and Ultrahigh Capacity Sodium Metal Anode, Nano Lett. 20 (2020) 7700–7708. https://doi.org/10.1021/acs.nanolett.0c03215.

[10] X. He, S. Jin, L. Miao, Y. Cai, Y. Hou, H. Li, K. Zhang, Z. Yan, J. Chen, A 3D Hydroxylated MXene/Carbon Nanotubes Composite as a Scaffold for Dendrite-Free Sodium-Metal Electrodes, Angew. Chemie Int. Ed. 59 (2020) 16705–16711. https://doi.org/10.1002/anie.202006783.

[11] Y. Fang, R. Lian, H. Li, Y. Zhang, Z. Gong, K. Zhu, K. Ye, J. Yan, G. Wang, Y. Gao, Y. Wei, D. Cao, Induction of Planar Sodium Growth on MXene ($Ti_3C_2T_x$)-Modified Carbon Cloth Hosts for Flexible Sodium Metal Anodes, ACS Nano. 14 (2020) 8744–8753.

https://doi.org/10.1021/acsnano.0c03259.

[12] H. Shi, M. Yue, C.J. Zhang, Y. Dong, P. Lu, S. Zheng, H. Huang, J. Chen, P. Wen, Z. Xu, Q. Zheng, X. Li, Y. Yu, Z.-S. Wu, 3D Flexible, Conductive, and Recyclable $Ti_3C_2T_x$ MXene-Melamine Foam for High-Areal-Capacity and Long-Lifetime Alkali-Metal Anode, ACS Nano. 14 (2020) 8678–8688. https://doi.org/10.1021/acsnano.0c03042.

[13] H. Jiang, X. Lin, C. Wei, Y. Zhang, J. Feng, X. Tian, Sodiophilic Mg^{2+}-Decorated Ti_3C_2 MXene for Dendrite-Free Sodium Metal Batteries with Carbonate-Based Electrolytes, Small. 18 (2022) 2107637. https://doi.org/10.1002/smll.202107637.

[14] S. Wang, Y. Liu, K. Lu, W. Cai, Y. Jie, F. Huang, X. Li, R. Cao, S. Jiao, Engineering rGO/MXene Hybrid Film as an Anode Host for Stable Sodium-Metal Batteries, Energy & Fuels. 35 (2021) 4587–4595. https://doi.org/10.1021/acs.energyfuels.0c04408.

[15] X.Y. Cui, Y.J. Wang, H.D. Wu, X.D. Lin, S. Tang, P. Xu, H.G. Liao, M. Sen Zheng, Q.F. Dong, A Carbon Foam with Sodiophilic Surface for Highly Reversible, Ultra-Long Cycle Sodium Metal Anode, Adv. Sci. 8 (2021) 2003178. https://doi.org/10.1002/advs.202003178.

[16] G. Wang, Y. Zhang, B. Guo, L. Tang, G. Xu, Y. Zhang, M. Wu, H.K. Liu, S.X. Dou, C. Wu, C. Wu, Core-Shell C@Sb Nanoparticles as a Nucleation Layer for High-Performance Sodium Metal Anodes, Nano Lett. 20 (2020) 4464–4471. https://doi.org/10.1021/acs.nanolett.0c01257.

[17] B. Zhang, G. Rousse, D. Foix, R. Dugas, D.A.D. Corte, J.M. Tarascon, Microsized Sn as Advanced Anodes in Glyme-Based Electrolyte for Na-Ion Batteries, Adv. Mater. 28 (2016) 9824–9830. https://doi.org/10.1002/adma.201603212.

[18] A.P. Cohn, T. Metke, J. Donohue, N. Muralidharan, K. Share, C.L. Pint, Rethinking Sodium-Ion Anodes as Nucleation Layers for Anode-Free Batteries, J. Mater. Chem. A. 6 (2018) 23875–23884. https://doi.org/10.1039/C8TA05911J.

[19] K. Lee, Y.J. Lee, M.J. Lee, J. Han, J. Lim, K. Ryu, H. Yoon, B. Kim, B.J. Kim, S.W. Lee, A 3D Hierarchical Host with Enhanced Sodiophilicity Enabling Anode-Free Sodium-Metal Batteries, Adv. Mater. 34 (2022) 2109767. https://doi.org/10.1002/adma.202109767.

[20] T. Li, J. Sun, S. Gao, B. Xiao, J. Cheng, Y. Zhou, X. Sun, F. Jiang, Z. Yan, S. Xiong, Superior Sodium Metal Anodes Enabled by Sodiophilic Carbonized Coconut Framework with 3D Tubular Structure, Adv. Energy Mater. 11 (2021) 2003699. https://doi.org/10.1002/aenm.202003699.

[21] H. Li, H. Zhang, F. Wu, M. Zarrabeitia, D. Geiger, U. Kaiser, A. Varzi, S. Passerini, Sodiophilic Current Collectors Based on MOF-Derived Nanocomposites for Anode-Less Na-Metal Batteries, Adv. Energy Mater. 12 (2022) 2202293. https://doi.org/10.1002/aenm.202202293.